

Article

Aerodynamic Interference on Trim Characteristics of Quad-Tiltrotor Aircraft

Pan Zhou^{1,*}, Renliang Chen^{1,*}, Ye Yuan²  and Cheng Chi³

¹ National Key Laboratory of Science and Technology on Rotorcraft Aeromechanics, College of Aerospace Engineering, Nanjing University of Aeronautics and Astronautics, Nanjing 210016, China; zhou_pvtol@nuaa.edu.cn

² Department of Aerospace Engineering, Swansea University, Wales SA1 8EN, UK; ye.yuan@swansea.ac.uk

³ Alfred Gessow Rotorcraft Center, University of Maryland, College Park, MD 20742, USA; chi@umd.edu

* Correspondence: crlae@nuaa.edu.cn; Tel.: +86-13813870483

Abstract: The aerodynamic interference between the different components of quad-tiltrotor (QTR) aircraft were considered to analyze its influence on trim characteristics. A comprehensive method with the fixed-wake model was developed for multiple aerodynamic interactions, improving the accuracy of the flight dynamics analysis. Additionally, a more general control strategy was developed to tackle the redundant control issue of the QTR, improving its control efficiency by coordinating the authority relationship of various control surfaces across the flight range. Then, the trim features were calculated in the helicopter mode, conversion mode, and airplane mode, and the relevant results with and without interaction were compared. The results show that the aerodynamic interaction mainly influences the body's vertical force, longitudinal force, and pitching moment. Furthermore, there are significant differences between collective and longitudinal sticks and pitch attitudes. The interference plays a major role in helicopter and conversion modes with a less-than-30-degree tilt angle.

Keywords: quad tiltrotor; aerodynamic interference; flight dynamics model; control strategy; trim characteristics



Citation: Zhou, P.; Chen, R.; Yuan, Y.; Chi, C. Aerodynamic Interference on Trim Characteristics of Quad-Tiltrotor Aircraft. *Aerospace* **2022**, *9*, 262. <https://doi.org/10.3390/aerospace9050262>

Academic Editor: Mark Lowenberg

Received: 10 March 2022

Accepted: 10 May 2022

Published: 12 May 2022

Publisher's Note: MDPI stays neutral with regard to jurisdictional claims in published maps and institutional affiliations.



Copyright: © 2022 by the authors. Licensee MDPI, Basel, Switzerland. This article is an open access article distributed under the terms and conditions of the Creative Commons Attribution (CC BY) license (<https://creativecommons.org/licenses/by/4.0/>).

1. Introduction

The tiltrotor aircraft has become the research focus in the helicopter industry due to its capability to combine the operational advantages of the fixed-wing airplane and the helicopter, making it capable of both hover and high-speed flight [1,2]. However, continuous research for decades has already brought the tiltrotor aircraft to its maximum payload and performance limitations. Therefore, with the aim of further improving its loading capacity and performance requirement, the concept of the quad tiltrotor (QTR) was proposed by Bell Helicopter company [3]. The QTR configuration adopts two paralleling nacelle systems, allowing its maximum takeoff weight to be as much as 70,000 kg, similar to the C-130J aircraft.

During the flight of the quad-tiltrotor aircraft, there are significant aerodynamic interactions that would influence its flight dynamic characteristics, including interference inside the multirotor system and the interaction between rotors and wings. Many researchers have implemented different methods to determine the aerodynamic interference, which is usually based on wind tunnel experiments [4–9] and CFD calculations [10–12]. The wind tunnel experiments suffer from extensive time and financial cost, and the CFD method requires high computational cost, making it unsuitable for QTR flight dynamic modelling and analysis. On the other hand, the empirical factor embedded fixed-wake method provides an alternative, more efficient method to quantify the aerodynamic interference of the QTR, which has the capability of synthesizing multiple interactions and has been widely used in the twin-tiltrotor aircraft [13] and tandem helicopter [14,15]. As a result, a more accurate aerodynamic model can be established based on this method to investigate the flight dynamics characteristics of QTR.

Furthermore, the control strategy is another critical issue for the QTR aircraft. Reasonable control allocation is the basis for the QTR to convert to safely during flight. The control allocation of the twin-tiltrotor can be directly determined by the tilt angle. The hybrid control equations in the longitudinal plane are established in Reference [16]. The attitude angle and the pilot workload are taken into the performance index to obtain the controlled displacement of the stick by using the optimal control method. However, the control redundancy of a quad-tiltrotor aircraft is much more complicated than that of the twin tiltrotor, and its control power is more sensitive to the aerodynamic characteristics in different flight ranges. In Reference [17], the control channels are decoupled to control surfaces, and the speed and height controllers are designed to determine the distribution coefficients of each surface. This method needs to be combined with the control system, which is not suitable for the analysis of flight dynamics.

In light of the preceding discussion, a more accurate aerodynamic model was established, which takes the interference of rotor–rotor and rotor–wing into account based on the synthesis of the empirical factor and fixed-wake method. The developed method is more appropriate for the analysis of flight dynamics. Aiming at the control redundancy problem, a general control strategy for the QTR aircraft is proposed to ensure that the flight dynamics characteristics and safety are satisfied across the flight range.

2. Flight Dynamics Model and Validation

The flight dynamics model is composed of the aerodynamic models of each component, including the rotor, wing, fuselage, and vertical fin. In this article, the model was developed based on the QTR configuration as shown in Figure 1, which was designed and manufactured by the laboratory at Nanjing University of Aeronautics and Astronautics. It can be seen that the rotors are installed at both ends of the front and rear wings, and the rotors can tilt with the nacelle around the axis. In the four rotors, the rotational directions of the diagonal rotors are the same, while the adjacent is opposite. The rotors are numbered 1, 2, 3, 4, and rotor 1 is right-handed. The flaperons are adopted on each wing surface, and they can be activated collaboratively and differentially to represent the function of the aileron and the elevator. The rudder is installed on the vertical fin to provide heading control. The general parameters of the quad tiltrotor can be seen in Table 1.

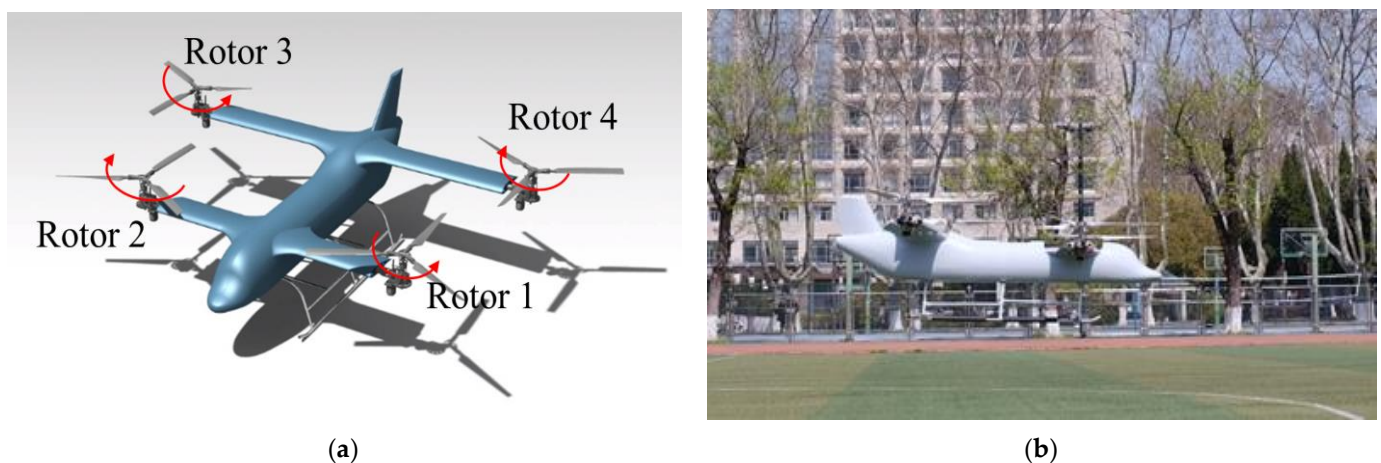


Figure 1. Configuration of the QTR. (a) Three-dimensional model of QTR. (b) Hover state of QTR flight test.

Table 1. General parameters of the quad tiltrotor.

Parameters	Values	Parameters	Values
gross weight/kg	60	rotor solidity ratio	0.0938
rotor rotational speed/rpm	2100	motor valuable power for rotors/kw	4.8×4
number of blades	3	mean chord of wing/m	0.3
rotor radius/m	0.58	distance between front and rear wings/m	1.2
blade chord/m	0.057	fuselage length/m	2
front wing span/m	1.6	fuselage width/m	2.6
rear wing span/m	2.2	fuselage height/m	0.5

In the flight dynamics modeling, the definition of the coordinate systems is shown in Figure 2.

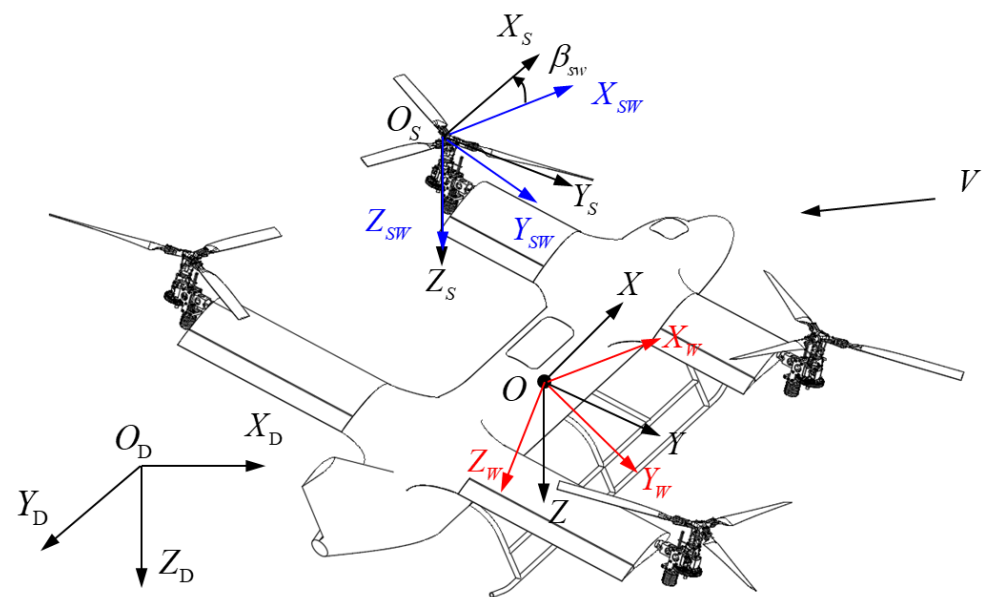


Figure 2. Definition of coordinate systems. where O is the center of gravity of the QTR; V is the inflow velocity; $O_D X_D Y_D Z_D$ is the inertial coordinate system; $OXYZ$ is the body coordinate system; $O_W X_W Y_W Z_W$ is the wind axis; $O_S X_S Y_S Z_S$ is the rotor fixed axis coordinate; $O_{SW} X_{SW} Y_{SW} Z_{SW}$ is the rotor wind coordinate, in which $O_{SW} X_{SW}$ is the projection of the velocity V onto the $O_{SW} X_{SW} Y_{SW}$ plane; β_{sw} , the side-slip angle of the rotor is the angle between $O_S X_S$ axis and $O_{SW} X_{SW}$ axis.

2.1. Rotor Model

The rotor aerodynamics model was developed considering the rotor dynamics characteristics, the induced inflow, and the aerodynamics interaction between the multirotor system. The flapping characteristics of the rotor blade were modeled based on Reference [18]. The modified Ferguson model [13] was used to represent the dimensionless induced velocity, as shown in the following equation:

$$\bar{v}_i = \frac{C}{\sqrt{0.866\lambda^2 + \mu^2} + \frac{0.6|C_{TW}|^{1.5}(|C_{TW}| - 8/3\lambda|\lambda|)}{(|C_{TW}| + 8\mu^2)(|C_{TW}| + 8\lambda^2)}} \tag{1}$$

where $C = C_{TW}/(2B^2)$, B is the blade tip-root loss factor; C_{TW} is the coefficient of the rotor thrust; μ is the advance ratio of the rotor; λ is the inflow ratio of the rotor, which is expressed by Equation (2):

$$\lambda = \bar{v}_i - \frac{w_S}{\Omega R} \tag{2}$$

where w_S is the hub vertical velocity in the rotor fixed axis coordinate; Ω is the rotational speed of the rotor; R is the rotor radius.

The blade flapping motion is described in the form of first-order Fourier series, and then the derivation of the tip-path plane dynamic equation can be calculated by the following equations [18].

$$\begin{bmatrix} \ddot{a}_0 \\ \ddot{a}_1 \\ \ddot{b}_1 \end{bmatrix} + D_R \begin{bmatrix} \dot{a}_0 \\ \dot{a}_1 \\ \dot{b}_1 \end{bmatrix} + K_R \begin{bmatrix} a_0 \\ a_1 \\ b_1 \end{bmatrix} = f_R \tag{3}$$

where a_0, a_1, b_1 are the flapping coefficients; D_R is the rotor damping matrix; K_R is the rotor rigidity matrix; f_R is the rotor incentive vector.

According to the induced velocity of the rotor and the flapping motion of the blade, the diagram of solving the rotor model is shown in Figure 3. The details of the procedure can be obtained in the References [18,19].

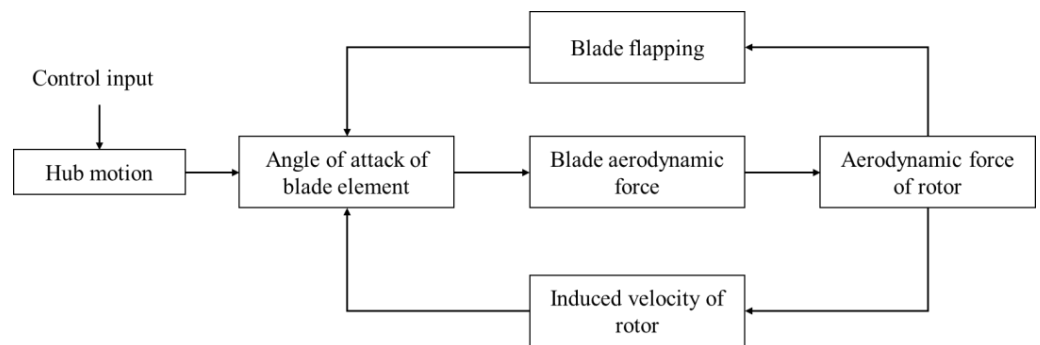


Figure 3. Diagram of solving the rotor model.

Then, the corresponding forces and moments acting on the center of gravity of the aircraft in the body coordinate system can be calculated using Equations (4) and (5), respectively.

$$\begin{bmatrix} X_{MR} \\ Y_{MR} \\ Z_{MR} \end{bmatrix} = T_S^B \begin{bmatrix} \cos \beta_{sw} & -\Delta \cdot \sin \beta_{sw} & 0 \\ \Delta \cdot \sin \beta_{sw} & \cos \beta_{sw} & 0 \\ 0 & 0 & 1 \end{bmatrix} \begin{bmatrix} -\rho(\Omega R)^2 \pi R^2 C_{HW} \\ \Delta \cdot \rho(\Omega R)^2 \pi R^2 C_{YW} \\ -\rho(\Omega R)^2 \pi R^2 C_{TW} \end{bmatrix} \tag{4}$$

$$\begin{bmatrix} L_{MR} \\ M_{MR} \\ N_{MR} \end{bmatrix} = T_S^B \begin{bmatrix} \cos \beta_{sw} & -\Delta \cdot \sin \beta_{sw} & 0 \\ \Delta \cdot \sin \beta_{sw} & \cos \beta_{sw} & 0 \\ 0 & 0 & 1 \end{bmatrix} \begin{bmatrix} \Delta \cdot L_W \\ M_W \\ \Delta \cdot Q \end{bmatrix} + \begin{bmatrix} 0 & -z_H & y_H \\ z_H & 0 & -x_H \\ -y_H & x_H & 0 \end{bmatrix} \begin{bmatrix} X_{MR} \\ Y_{MR} \\ Z_{MR} \end{bmatrix} \tag{5}$$

where Δ denotes the rotation direction of the rotor, in which $\Delta = 1$ represents right-handed and $\Delta = -1$ represents left-handed; the definition of β_{sw} is shown in Figure 2; ρ is the air density; C_{HW}, C_{YW}, C_{TW} are the rotor coefficients of backward force, sideward force, and thrust respectively, whose calculation formulas can be seen in Reference [18]. Q is the rotor shaft torque; L_W is the hub moment in the rolling channel; M_W is the hub moment in the pitching channel; $(x_H, y_H, z_H)^T$ is the vector of the rotor hub relative to the center of gravity.

The aerodynamic interference between the multi-rotor system could significantly alter the flight dynamics characteristics across the flight range, which should be considered in the rotor modelling process. Based on References [13,14], this interference can be divided into two aspects, namely, the lateral interaction and the longitudinal interaction. The formation of the lateral interaction shares many similarities with the twin-rotor interaction in the tiltrotor aircraft, and the longitudinal interaction is similar to the rotor interaction in the tandem helicopter. The corresponding interaction between different rotors in the QTR configuration is shown in Table 2.

Table 2. Categories of rotor–rotor interaction.

Rotor Number	1	2	3	4
1	—	Lateral	—	Longitudinal
2	Lateral	—	Longitudinal	—
3	—	Longitudinal	—	Lateral
4	Longitudinal	—	Lateral	—

In Table 2, the long dash “—” means ignoring the interaction of these two rotors. It can be seen that the lateral rotor interaction includes the interference between rotor 1 and rotor 2, and interference between rotor 3 and rotor 4. The longitudinal rotor interaction contains the aerodynamic interference between rotor 1 and rotor 4 and interference between rotor 2 and rotor 3.

2.1.1. Lateral Interaction

The lateral interaction would add additional induced velocity on the rotor disc, which can be calculated using the lateral interaction factor, X_S , which is shown in Equation (6).

$$X_S = X_{SF} + X_{SS} \tag{6}$$

where X_{SF} is the side-by-side-induced velocity coefficient in the forward flight of the aircraft, determined by the rotor advance ratio μ . X_{SS} is the sideward flight-induced velocity coefficient, decided by the lateral velocity advance ratio. The calculation equations can be written as follows.

$$\begin{aligned} X_{SF,L} &= f_{SF}(|\mu_L|) \\ X_{SF,R} &= f_{SF}(|\mu_R|) \end{aligned} \tag{7}$$

if $v_{H,L} + v_{H,R} \geq 0$:

$$X_{SS,L} = f_{SS}\left(\left|\frac{v_{H,L} + v_{H,R}}{2\Omega R}\right|\right), \quad X_{SS,R} = 0 \tag{8}$$

otherwise:

$$X_{SS,L} = 0, \quad X_{SS,R} = f_{SS}\left(\left|\frac{v_{H,L} + v_{H,R}}{2\Omega R}\right|\right) \tag{9}$$

where μ_L, μ_R are the advanced ratios of the left and right rotors respectively; $v_{H,L}, v_{H,R}$ are the lateral velocity at the hub of the left and right rotors respectively. Therefore, the velocity increment provided by the lateral interaction is calculated based on Equation (10)

$$\Delta\bar{v}_{i,S} = X_S \cdot \bar{v}_i \tag{10}$$

where v_i can be obtained from Equation (1).

2.1.2. Longitudinal Interaction

The longitudinal interaction is more complicated than the lateral one as the nacelle incidence angle would play a major effect on the interaction scheme. Therefore, the relevant calculation method should coordinate the interaction phenomena in different modes (helicopter mode, conversion mode, and airplane mode).

For helicopter mode, front rotor interference factor $X_{H,F}$ and rear rotor interference factor $X_{H,B}$ can be written as follows, respectively [14]:

$$X_{H,F} = \eta_{FR} \left[\left(-0.151\chi_B - 0.314\chi_B^2 + 0.164\chi_B^3 \right) (1 - |\sin\beta_{SW,B}|) + \left(0.0131\chi_B - 0.0764\chi_B^2 - 0.0085\chi_B^3 \right) |\sin\beta_{SW,B}| \right] \tag{11}$$

$$X_{H,B} = \eta_{FR} \left[\left(0.321\chi_F - 0.368\chi_F^2 + 0.492\chi_F^3 \right) (1 - |\sin\beta_{SW,F}|) + \left(0.0131\chi_F - 0.0764\chi_F^2 - 0.0085\chi_F^3 \right) |\sin\beta_{SW,F}| \right] \tag{12}$$

where χ_F and χ_B represent the wake angles of the front and rear rotors, respectively. β_{SW} is the angle of the side-slip of the rotor. η_{FR} is the relative position factor of the front-rear

rotor interference, determined by the projection relationship between front and rear rotor, as shown in Equation (13).

$$\eta_{FR} = \frac{S_{FR}}{\pi R^2} = \frac{\left(\pi - \arccos \frac{R - l_{RRL}}{R}\right) R^2 + \sqrt{2Rl_{RRL} - l_{RRL}^2}}{\pi R^2} \tag{13}$$

where l_{RRL} is the lateral distance between the centre of the front and rear rotors, S_{FB} is the area of the shaded part, as shown in Figure 4a. Thus, the corresponding induced velocity increments can be written as:

$$\begin{aligned} \Delta \bar{v}_{i,HF} &= X_{H,F} \bar{v}_{i,B} \\ \Delta \bar{v}_{i,HB} &= X_{H,B} \bar{v}_{i,F} \end{aligned} \tag{14}$$

where $v_{i,B}$ and $v_{i,F}$ represent induced velocities of front and rear rotors, respectively.

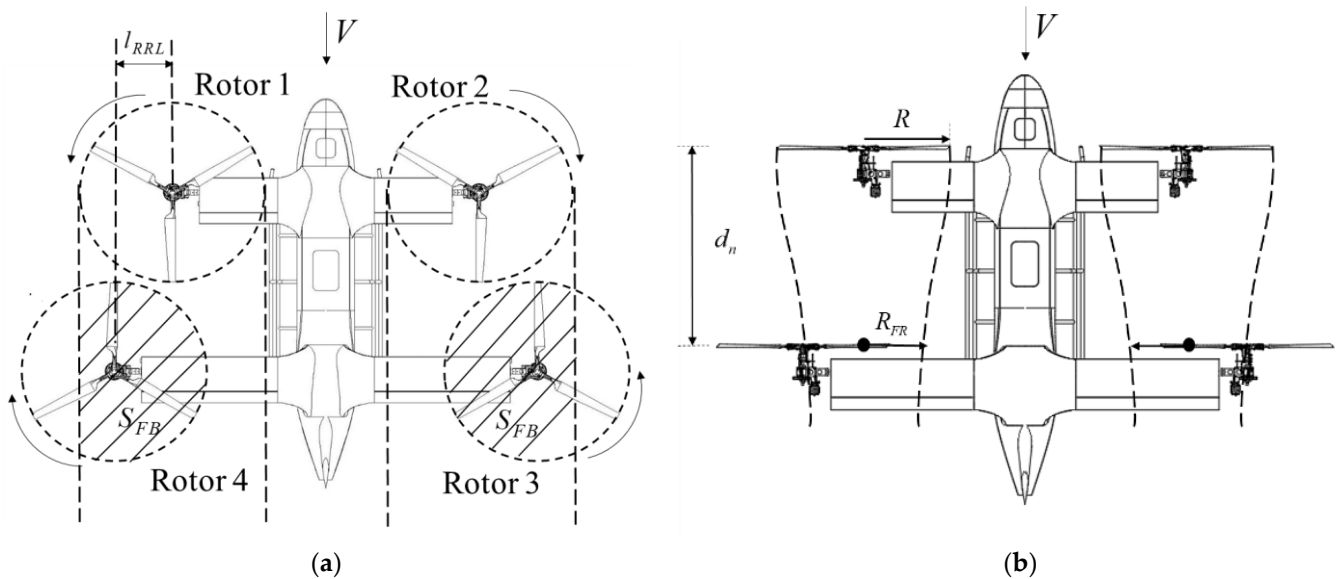


Figure 4. Interactional diagram of front rotor wake to the rear rotor. (a) Top view of longitudinal interaction (helicopter mode). (b) Top view of longitudinal interaction (airplane mode). where V is inflow velocity.

In airplane mode, the rear rotor cannot introduce a significant influence on the aerodynamics of the front rotor, and only the rear rotor can be impacted at this flight range. Therefore, based on the projection relationship in the airplane mode, the induced velocity increment of the rear rotor can be calculated using Equation (15).

$$\Delta \bar{v}_{i,AB} = \eta_{FR} \frac{R^2}{R_{FR}^2} \bar{v}_{i,F} \tag{15}$$

where R_{FR} is the influential area radius of the front rotor wake at the rear rotor disc, as shown in Figure 4b, and it can be calculated as follows.

$$R_{FR} = R \left[0.78 + 0.22e^{-(0.3+2L_n\sqrt{C_{HST}}+60C_{HST})} \right] \tag{16}$$

$$C_{HST} = \sqrt{C_H^2 + C_S^2 + C_T^2}, \quad L_n = d_n / R \tag{17}$$

where C_H , C_S , C_T are the coefficient of the backward force, sideward force, and thrust of the rotor system, respectively. d_n is the longitudinal distance between the centre of the front and rear rotors.

In the conversion mode, the interaction can be calculated using the fitting method to combine the results in the helicopter mode and airplane mode based on the tilt angle β_N , which can be expressed as:

$$\begin{aligned}\Delta\bar{v}_{i,TB} &= \Delta\bar{v}_{i,HF}(1 - \sin\beta_N) \\ \Delta\bar{v}_{i,TF} &= \Delta\bar{v}_{i,AB}\sin\beta_N + \Delta\bar{v}_{i,HB}(1 - \sin\beta_N)\end{aligned}\quad (18)$$

2.2. Wing Model

In the flight of the quad-tiltrotor aircraft, the downwash of the rotor directly impacts the wing's surface, which will generate an additional aerodynamic load. Reference [20] has indicated that the download to the wing generated from the rotor can reach 10~15% of the rotor's thrust of a tiltrotor aircraft in the hover state. For the quad-tiltrotor aircraft, this downwash effect can be summarized as two types, including the rotor downwash effect on its connected wing (Type 1), and the downwash interference on its unattached wing (Type 2).

2.2.1. Rotor-Wing Interaction: Type 1

To quantify this rotor-wing interaction, the wing can be divided into two parts: the area affected by the rotor wake, i.e., the slipstream area; the area unaffected by the rotor wake, called the freestream area. The resultant aerodynamic force of the wing is the superposition of the two aerodynamic forces. The areas of slipstream and freestream can be calculated as follows [21].

$$\begin{aligned}S_{WS} &= S_{Smax} \left\{ \left[1.386 \left(\frac{\pi}{2} - \beta_N \right) \right] + \cos \left[3.114 \left(\frac{\pi}{2} - \beta_N \right) \right] \right\} \frac{\mu_{max} - \mu}{\mu_{max}} \\ S_{WF} &= S_W - S_{WS} \\ S_{Smax} &= 2R_i c\end{aligned}\quad (19)$$

where the subscript *WS* represents the slipstream area. *WF* represents the freestream area. μ_{max} is the maximum advanced ratio of the rotor while the wake phasing out the upper connected wing. R_i is the influential area radius of the rotor wake at the connected wing. c is the mean chord of the wing. S_W is the total area of the wing.

The flow velocity of the slipstream can be expressed as:

$$\begin{bmatrix} u_{WWS} \\ v_{WWS} \\ w_{WWS} \end{bmatrix} = \begin{bmatrix} u + \frac{R^2}{R_i^2} \bar{v}_i \sin\beta_N \cdot \Omega R \\ v \\ w - \frac{R^2}{R_i^2} \bar{v}_i \cos\beta_N \cdot \Omega R \end{bmatrix} + \boldsymbol{\omega} \times \mathbf{r}_{WWS}\quad (20)$$

where \mathbf{r}_{WWS} is the aerodynamic centre of the slipstream area.

2.2.2. Rotor-Wing Interaction: Type 2

The schematic diagram of the rotor downwash interference on its unattached wing is shown in Figure 5. The cross effect of the rotor-wing interaction (Rotor 1 downwash on the wing connecting Rotor 3) is ignored due to it being minimal compared to other influences. The interaction of the rear rotor with the front wing only exists when the aircraft flies backwards, and its calculation method is the same as the method shown below.

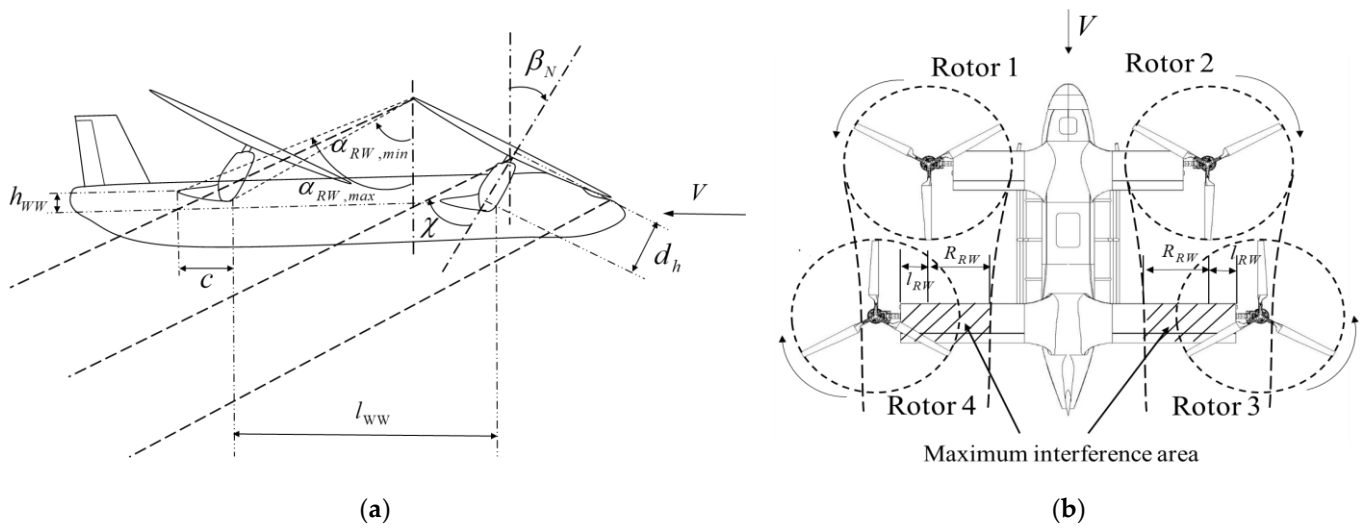


Figure 5. Interactional diagram of front rotor wake to the rear wing. (a) Side view of interference. (b) Top view of interference.

The side view of the interference is illustrated in Figure 5a, in which $\alpha_{RW,min}$ is the critical angle of the front rotor that starts to interfere with the rear wing; $\alpha_{RW,max}$ is the angle that the rear wing starts to be entirely immersed in the wake of the front rotor; h_{WW} is the height difference of the front-rear wings; l_{WW} is the longitudinal distance between the front and rear wings; d_h is the distance between the rotor hub centre and the tilting axis. Therefore, the relevant angles can be calculated using the following equations.

$$\begin{cases} \tan \alpha_{RW,min} = \frac{l_{WW} - 0.25c - (R \cos \beta_N - d_h \sin \beta_N)}{R \sin \beta_N + d_h \cos \beta_N - h_{WW}} \\ \tan \alpha_{RW,max} = \frac{l_{WW} + 0.75c - (R \cos \beta_N - d_h \sin \beta_N)}{R \sin \beta_N + d_h \cos \beta_N - h_{WW}} \end{cases} \quad (21)$$

The top view of the interference is illustrated in Figure 5b, representing the maximum interference area of the front rotor to the rear wing. When $\beta_N + \chi \geq \alpha_{RW,min}$, the wake of the front rotor alters the aerodynamics of the rear wing, the corresponding interference area S_{RW} can be calculated by the following equations.

$$\begin{aligned} S_{RW} &= 0, & \beta_N + \chi &< \alpha_{RW,min} \\ S_{RW} &= 2(l_{RW} + R_{RW})c \cdot \frac{\beta_N + \chi - \alpha_{RW,min}}{\alpha_{RW,max} - \alpha_{RW,min}}, & \alpha_{RW,min} &\leq \beta_N + \chi < \alpha_{RW,max} \\ S_{RW} &= 2(l_{RW} + R_{RW})c, & \alpha_{RW,max} &\leq \beta_N + \chi \end{aligned} \quad (22)$$

where l_{RW} is the lateral distance from the outer end of the rear wing to the hub of the front rotor; R_{RW} is the contraction radius of the front rotor wake at the rear wing. The correction of the flow velocity affected by this interference can be written as:

$$\begin{bmatrix} \Delta u_{WR} \\ \Delta v_{WR} \\ \Delta w_{WR} \end{bmatrix} = \begin{bmatrix} \bar{v}_{i,F} \frac{R^2}{R_{RW}^2} \sin(\beta_N + \chi) \cdot \Omega R \\ 0 \\ -\bar{v}_{i,F} \frac{R^2}{R_{RW}^2} \cos(\beta_N + \chi) \cdot \Omega R \end{bmatrix} \quad (23)$$

The dynamic pressure of the slipstream q_{WS} and the freestream q_{WF} can be calculated considering this effect. Then, the resultant forces and moments of the wing component can be expressed as:

$$\begin{aligned} \tilde{L}_W &= q_{WS} S_{WS} C_{L,WS} + q_{WF} S_{WF} C_{L,WF} \\ D_W &= q_{WS} S_{WS} C_{D,WS} + q_{WF} S_{WF} C_{D,WF} \\ M_W &= q_{WS} S_{WS} c C_{M,WS} + q_{WF} S_{WF} c C_{M,WF} \end{aligned} \quad (24)$$

where \tilde{L}_W is the lift of the wing; D_W is the drag of the wing; M_W is the pitching moment of the wing; C_L, C_D, C_M are the lift, drag, and pitching moment coefficients, respectively, which are related to the Mach number and configuration of the flaperons. Therefore, the forces $(X_W, Y_W, Z_W)^T$ and moments $(L_W, M_W, N_W)^T$ produced by the wing in the body coordinate system can be obtained through coordination transformation.

2.3. Model of Other Components

Other aerodynamic components in the model include the fuselage and the vertical fin. The fuselage aerodynamics was obtained by CFD using the fitting method. The detailed introduction of the method is shown in reference [22] and was verified by the experiment. In brief, the ansys-icem is used to mesh grid and the ansys-fluent is used for calculation. The number of boundary layers on the fuselage is 10. The normal height ratio of meshes along the wall is 1.15, and the total meshes are 4 million. The k- ω shear stress transport (SST) turbulence model was employed, and the SIMPLE algorithm was used to solve the model.

Thus, the resultant aerodynamic force coefficients $C_{LF}, C_{DF}, C_{YF}, C_{RF}, C_{MF}, C_{NF}$, related to the angle of attack and side-slip of the aircraft, can be obtained. Figure 6 indicates the numerical simulation of the fuselage aerodynamics.

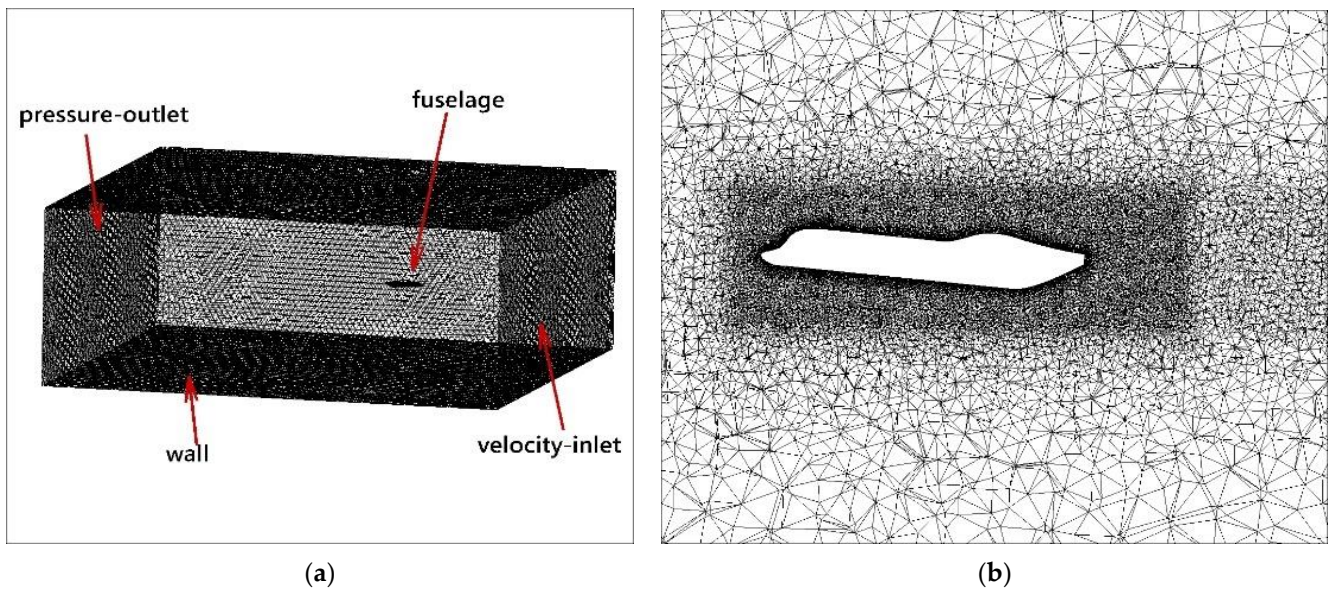


Figure 6. Numerical simulation of the fuselage aerodynamics. (a) Overall meshing. (b) Mesh details.

At last, the aerodynamics of the fuselage in the body coordinate can be expressed as follows.

$$\begin{bmatrix} X_F \\ Y_F \\ Z_F \end{bmatrix} = T_W^B \begin{bmatrix} -q_{F\infty} S_F C_{DF} \\ q_{F\infty} S_F C_{YF} \\ -q_{F\infty} S_F C_{LF} \end{bmatrix} \quad (25)$$

$$\begin{bmatrix} L_F \\ M_F \\ N_F \end{bmatrix} = T_W^B \begin{bmatrix} q_{F\infty} S_F l_F C_{RF} \\ q_{F\infty} S_F l_F C_{MF} \\ q_{F\infty} S_F l_F C_{NF} \end{bmatrix} + \begin{bmatrix} 0 & -z_F & y_F \\ z_F & 0 & -x_F \\ -y_F & x_F & 0 \end{bmatrix} \begin{bmatrix} X_F \\ Y_F \\ Z_F \end{bmatrix} \quad (26)$$

where $q_{F\infty}$ is the local dynamic pressure; S_F is the flat plate area of the fuselage; l_F is the characteristic length of the fuselage; T_W^B is the transfer matrix from the wind coordinate to the body coordinate; $(x_F, y_F, z_F)^T$ is the distance from the aerodynamic centre of the fuselage to the centre of gravity.

The vertical fin aerodynamics are decided by the lift coefficient C_{LVT} and the drag coefficient C_{DVT} . Thereby, the resultant aerodynamic force can be obtained in the body coordinate.

$$\begin{bmatrix} X_{VT} \\ Y_{VT} \\ Z_{VT} \end{bmatrix} = \begin{bmatrix} \cos(\alpha_{VT} - i_{VT}) \cos \beta_{VT} & \sin \beta_{VT} & \sin(\alpha_{VT} - i_{VT}) \cos \beta_{VT} \\ -\cos(\alpha_{VT} - i_{VT}) \sin \beta_{VT} & \cos \beta_{VT} & -\sin(\alpha_{VT} - i_{VT}) \sin \beta_{VT} \\ -\sin(\alpha_{VT} - i_{VT}) & 0 & \cos(\alpha_{VT} - i_{VT}) \end{bmatrix} \cdot \begin{bmatrix} -q_{VT\infty} S_{VT} C_{DVT} \\ -q_{VT\infty} S_{VT} C_{LVT} \\ 0 \end{bmatrix} \quad (27)$$

$$\begin{bmatrix} L_{VT} \\ M_{VT} \\ N_{VT} \end{bmatrix} = \begin{bmatrix} 0 & -z_{VT} & y_{VT} \\ z_{VT} & 0 & -x_{VT} \\ -y_{VT} & x_{VT} & 0 \end{bmatrix} \begin{bmatrix} X_{VT} \\ Y_{VT} \\ Z_{VT} \end{bmatrix} \quad (28)$$

where $q_{VT\infty}$ is the local dynamic pressure; S_{VT} is the area of the vertical fin; i_{VT} is the incidence of the vertical fin; β_{VT} is the side-slip angle of the vertical fin; α_{VT} is the angle of attack.

2.4. Integrated Equations of the Vehicle

The whole model has 16 degrees of freedom, and its general nonlinear equations of motion take the form [23]:

$$\dot{x} = f(x, \delta_S, t) \quad (29)$$

in which x is the state vector,

$$x = \left[u, v, w, p, q, r, \varphi, \theta, \psi, v_{0,LF}, v_{0,RF}, v_{0,RB}, v_{0,LB}, \dot{a}_{0,LF}, \dot{a}_{1,LF}, \dot{b}_{1,LF}, a_{0,LF}, a_{1,LF}, b_{1,LF}, \dot{a}_{0,RF}, \dot{a}_{1,RF}, \dot{b}_{1,RF}, a_{0,RF}, a_{1,RF}, b_{1,RF}, \dot{a}_{0,RB}, \dot{a}_{1,RB}, \dot{b}_{1,RB}, a_{0,RB}, a_{1,RB}, b_{1,RB}, \dot{a}_{0,LB}, \dot{a}_{1,LB}, \dot{b}_{1,LB}, a_{0,LB}, a_{1,LB}, b_{1,LB} \right]^T \quad (30)$$

where the subscript *LF* represents rotor 1, *RF* represents rotor 2, *RB* represents rotor 3, *LB* represents rotor 4; $u, v, w, p, q,$ and r are the rigid body translational velocity components and angular rates; $\varphi, \theta,$ and ψ are the rigid body Euler angles; v_0 is the induced velocity. δ_S is the control input vector,

$$\delta_S = \left[\delta_{col}, \delta_{lat}, \delta_{lon}, \delta_{ped} \right]^T \quad (31)$$

where δ_{col} is the collective stick displacement; δ_{lat} is the lateral stick displacement; δ_{lon} is the longitudinal stick displacement; δ_{ped} is the pedal displacement. The analysis of δ_S is detailed in chapter 3.

2.5. Validation

In order to validate the accuracy of the model established in the paper, the experiment of the thrust of the isolated rotor was carried out in the wind tunnel, whose test section size is 3.2 m × 2.4 m and the maximum wind speed is 50 m/s. The equipment of the isolated rotor test is shown in Figure 7a,b. The rotor test involves two aspects: one is the required power changing with the rotor thrust; the other is the rotor thrust changing with the flight velocity. The collective is set to 6°, 8°, 10°, 12°, and 14° for the first case, the wind speed is 0 m/s. The collective is fixed at 10° for the second case, the wind speed changes from 0 m/s to 16 m/s. To avoid the ground effect, the height from the ground of the rotor should not be less than 1.2 times its diameter.

Additionally, the rotor–wing interaction was implemented in the article. However, due to the restriction of the wind tunnel facilities, the interaction test only included rear rotors to the rear wing in the hover state, which can be seen in Figure 7c. The wing's download caused by the rotor thrust could be measured with different collective inputs that involve 6°, 8°, 10°, 12°, and 14°. In these two experiments, the rotor rotational speeds were set to be 2100 rpm. The comparisons between test and calculation are shown in Figure 8.

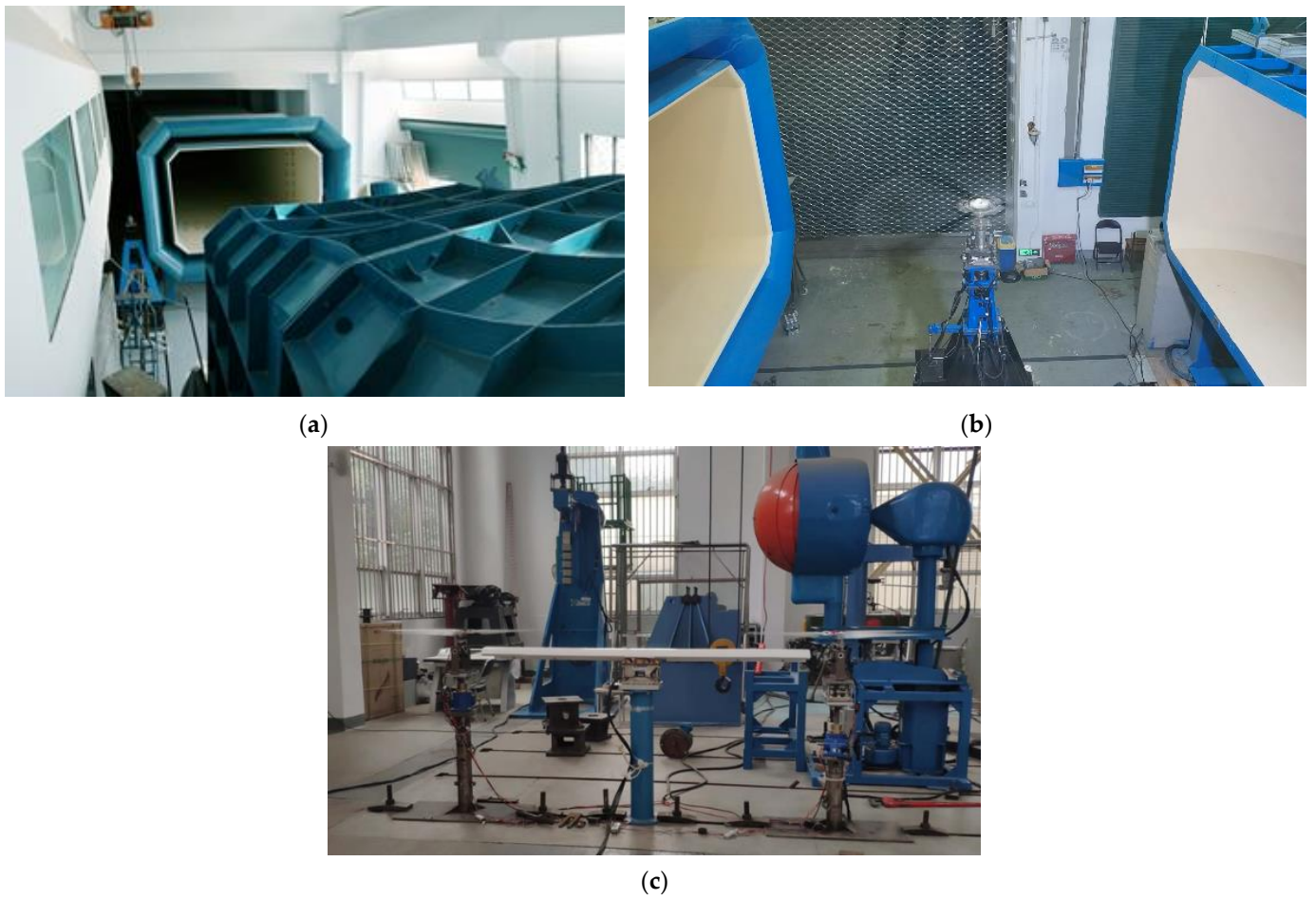


Figure 7. Experiment of the rotor thrust and the rotor–wing interaction. (a) The wind tunnel. (b) Experiment of the rotor thrust. (c) Experiment of the rotor–wing interaction.

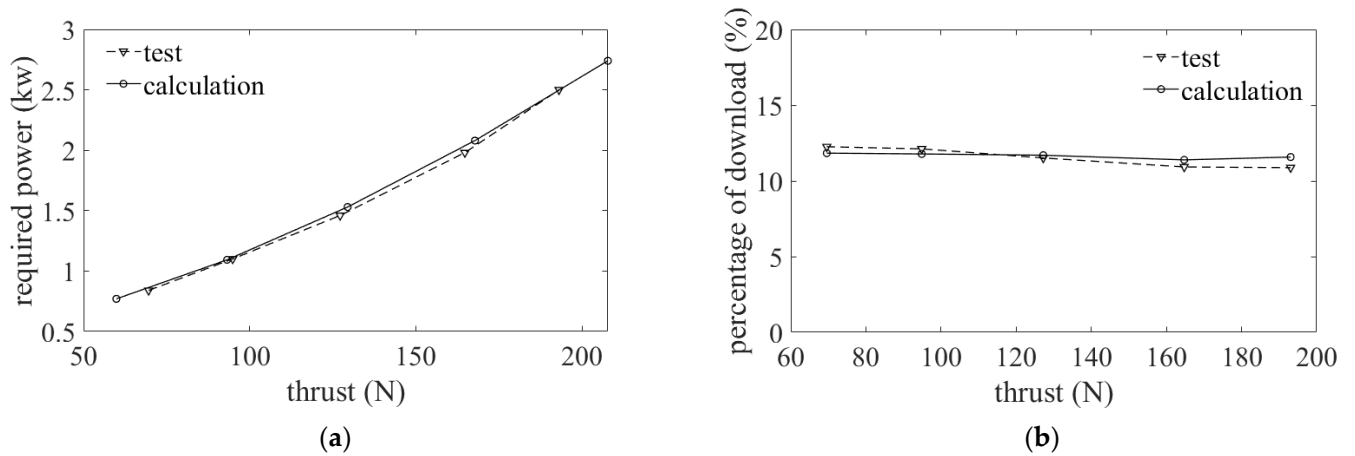


Figure 8. Cont.

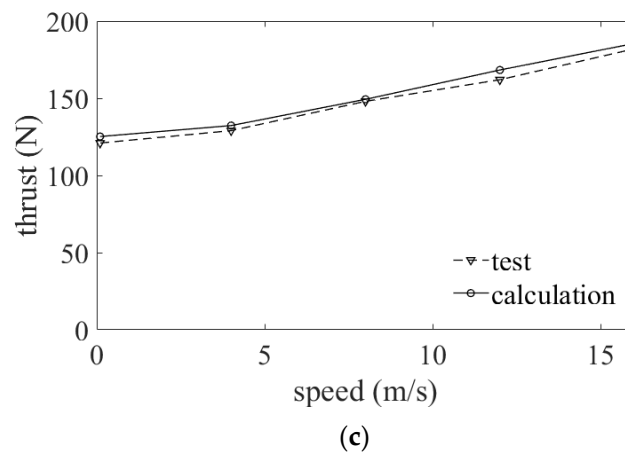


Figure 8. Comparisons between tests and calculations. (a) Required power of the isolated rotor. (b) Rotor thrust changes with velocity. (c) Percentages of wing's download to rotor thrust.

According to Figure 8, the results from the developed models were in good agreement with the experiment results, indicating the accuracy of the modeling method. The download of the wing accounts for approximately 12~13% of the rotor thrust in the hover state, consistent with that described in Reference [20]. To further improve the accuracy of the model, especially the aerodynamic interference during the maneuvering flight, the aircraft flight test was the research focus in the next step.

3. Control Strategy

The control strategy of the QTR is more complicated than other rotor-powered vehicles due to its redundant control characteristics. The control inputs of the QTR configuration are shown in Table 3.

Table 3. Forms and numbers of control inputs.

Components	Control Surface	Number
Rotor	Collective	$3 \times 4 = 12$
	Longitudinal cyclic	
	Lateral cyclic	
Wing	Flaperon	$2 \times 2 = 4$
Empennage	Rudder	1

As shown in Table 3, there are 17 control surfaces in the QTR configurations, indicating that this is an underdetermined system with more unknown variables than the number of equations in trimming.

When the quad-tiltrotor aircraft is flying in helicopter mode, the control efficiencies of the flaperon and rudder are relatively small. Therefore, the controllability is mainly provided by the rotor system. When the QTR is in conversion and airplane modes, the control efficiencies of the flaperon and rudder increase with tilting of the nacelle, and the rotor controllability decreases. Furthermore, the change of the tilt angle may lead to additional control coupling problems. Therefore, a mixed control strategy was proposed for the QTR configuration, which is shown below.

$$\delta = \begin{bmatrix} \delta_{ver_h} \cos \beta_N + \delta_T (1 - \cos \beta_N) \\ \delta_{lat_h} \cos \beta_N + \delta_a (1 - \cos \beta_N) \\ \delta_{lon_h} \cos \beta_N + \delta_e (1 - \cos \beta_N) \\ \delta_{yaw_h} \cos \beta_N + \delta_r (1 - \cos \beta_N) \end{bmatrix} \quad (32)$$

where $\delta_{ver_h}, \delta_{lat_h}, \delta_{lon_h}, \delta_{yaw_h}$ are the control input of vertical, lateral, longitudinal, and heading in helicopter mode, respectively. $\delta_T, \delta_a, \delta_e, \delta_r$ are the control inputs of throttle, lateral, longitudinal, and heading in airplane mode, respectively.

3.1. Strategy in the Helicopter Mode

In helicopter mode, the vertical channel is controlled by the combined collective with the four rotors. The lateral channel is achieved through the collective differential of left and right rotors. The longitudinal channel is achieved by the collective differential of front and rear rotors. The yawing channel is performed by the differential lateral cyclic pitch of front and rear rotors. Based on Equation (32), the control input in helicopter mode can be written as follows.

$$\delta_H = [\delta_{ver_h}, \delta_{lat_h}, \delta_{lon_h}, \delta_{yaw_h}]^T \tag{33}$$

The four control input variables are allocated to each rotor so that the corresponding collective, longitudinal cyclic pitch, and lateral cyclic pitch can be determined. Their relationships are shown in Table 4.

Table 4. Relationship between control value for each rotor and control input.

Control	Rotor 1	Rotor 2	Rotor 3	Rotor 4
Collective	$\delta_{ver_h} + \delta_{lat_h} - \delta_{lon_h}$	$\delta_{ver_h} - \delta_{lat_h} - \delta_{lon_h}$	$\delta_{ver_h} - \delta_{lat_h} + \delta_{lon_h}$	$\delta_{ver_h} + \delta_{lat_h} + \delta_{lon_h}$
Longitudinal cyclic	0	0	0	0
Lateral cyclic	δ_{yaw_h}	δ_{yaw_h}	$-\delta_{yaw_h}$	$-\delta_{yaw_h}$

It can be seen, in Table 4, the longitudinal motion is controlled by the collective differential of front and rear rotors, resulting in the longitudinal cyclic invariable in this mode. To unify the control inputs in different flight modes, the displacements of the sticks are set as the control inputs, and their variation ranges are from 0 to 1, as indicated as follows.

$$\delta_S = [\delta_{col}, \delta_{lat}, \delta_{lon}, \delta_{ped}]^T \tag{34}$$

Therefore, the relationship between the control input δ_H in helicopter mode and the displacement of the stick can be written as:

$$\delta_{ver_h} = k_{ver}(\delta_{col} - \delta_{col,n}) \tag{35}$$

$$\delta_{lat_h} = k_{lat}(\delta_{lat} - \delta_{lat,n}) \tag{36}$$

$$\delta_{lon_h} = k_{lon}(\delta_{lon} - \delta_{lon,n}) \tag{37}$$

$$\delta_{yaw_h} = k_{yaw}(\delta_{ped} - \delta_{ped,n}) \tag{38}$$

where $k_{ver}, k_{lat}, k_{lon}, k_{yaw}$ represent collective, lateral, longitudinal, and heading control coefficients in the helicopter mode, respectively. The constants $\delta_{col,n}, \delta_{lat,n}, \delta_{lon,n}$, and $\delta_{ped,n}$ are the neutral displacement of the stick.

3.2. Strategy in the Airplane Mode

In the airplane mode, the throttle control is achieved through the combined collective of the four rotors; the longitudinal and lateral control are conducted by the combined and differential flaperon of the wing; the heading is achieved by the rudder. According to Equation (32), the control input in airplane mode can be expressed as:

$$\delta_A = [\delta_T, \delta_a, \delta_e, \delta_r]^T \tag{39}$$

Therefore, the relationship between the control input δ_A in the airplane mode and the stick displacement can be written as follows.

$$\delta_T = k_{ver}(\delta_{col} - \delta_{col,n}) \tag{40}$$

$$\delta_a = k_a(\delta_{lon} - \delta_{lon,n}) \tag{41}$$

$$\delta_e = k_e(\delta_{lon} - \delta_{lon,n}) \tag{42}$$

$$\delta_t = k_t(\delta_{ped} - \delta_{ped,n}) \tag{43}$$

where k_a, k_e, k_t represent lateral, longitudinal, and heading control coefficients in the airplane mode.

To sum up, the control input in each mode is transformed into a function of the stick displacement so that the values of rotor collective, rotor cyclic pitch, flaperon, rudder, and attitude are unique, which can be obtained in the trim calculation. Thereby, the control redundant problem of the quad-tiltrotor aircraft is settled.

4. Results

The aerodynamic interference influence on the trim characteristics is investigated in this part. The relevant calculation points were selected from the conversion corridor which was calculated based on the method in Reference [24], as shown in Figure 9.

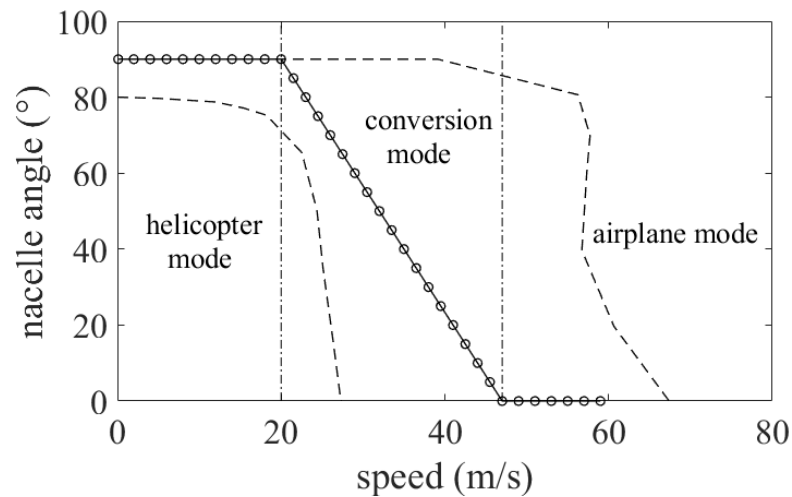


Figure 9. Conversion corridor of quad tiltrotor and selected trimming points.

At these trimming points, the vehicle is in equilibrium. In this case, the body resultant forces and moments are zero. Therefore, the body translational accelerations, angular rates, and angular accelerations of the vehicle are zero. Additionally, the flapping motion of the rotor maintains a steady state, and Equation (3) can be written as follows.

$$\mathbf{K}_R \begin{bmatrix} a_0 \\ a_1 \\ b_1 \end{bmatrix} - \mathbf{f}_R = \mathbf{0} \tag{44}$$

Combined with Equation (29), the Newton–Raphson algorithm is used to solve the equilibrium equations. The trim characteristics can be calculated with and without interference according to the procedure diagram shown in Figure 10.

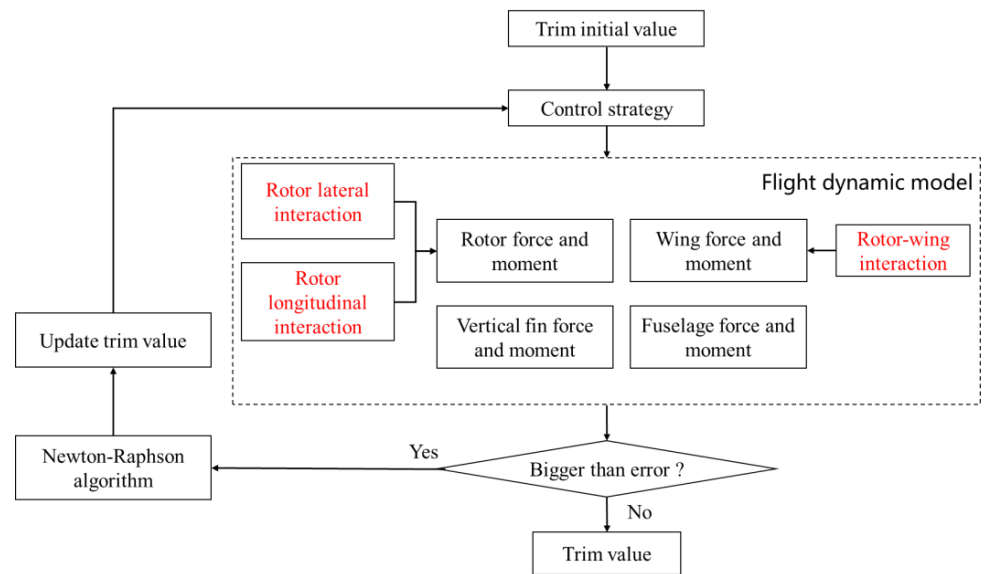


Figure 10. Diagram of the trim calculation procedure.

In Figure 10, the trim value includes collective stick, lateral stick, longitudinal stick, roll attitude, and pitch attitude. The red parts indicate the aerodynamic interactions, such as rotor lateral interaction, rotor longitudinal interaction, and rotor–wing interaction.

The trim calculation results are shown in Figure 11, which demonstrates that the aerodynamic interaction affects the trim results in the collective and longitudinal sticks and the pitch attitude. The lateral and heading sticks and roll attitudes are close to zero across the flight range.

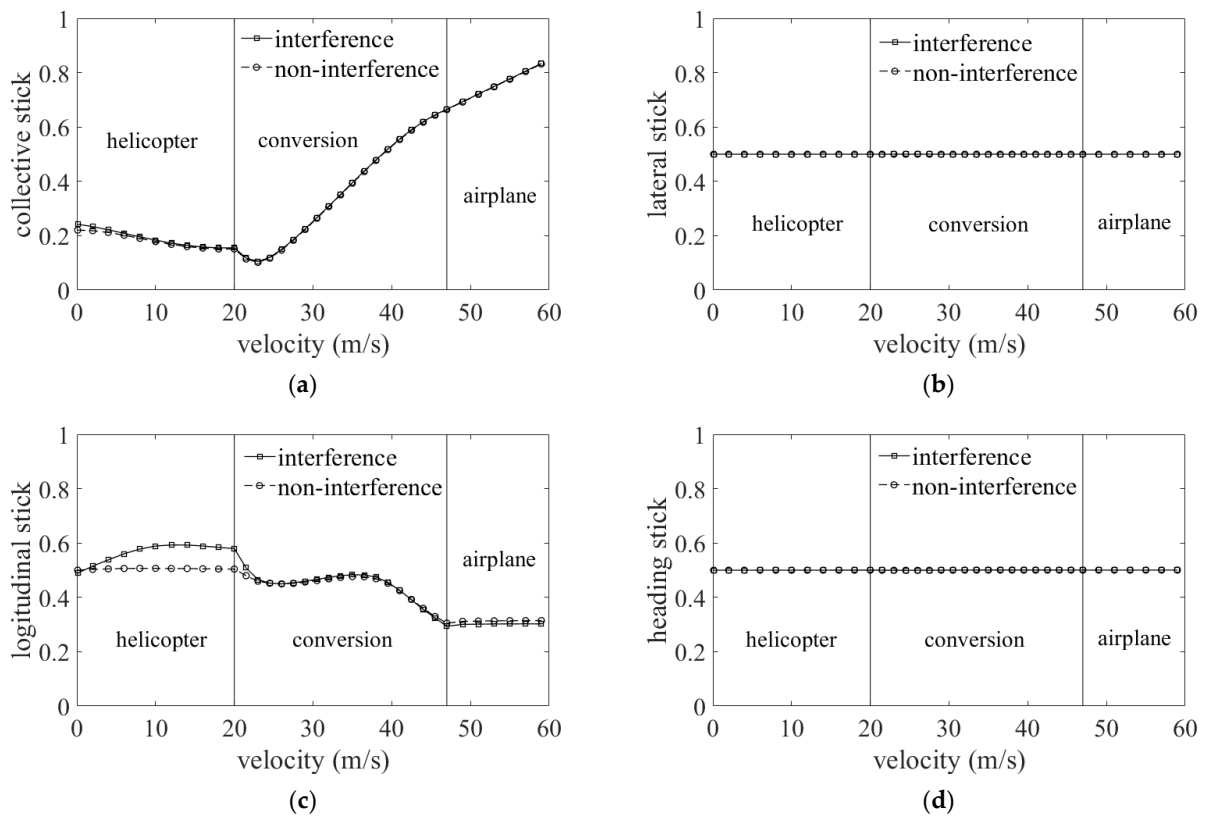


Figure 11. Cont.

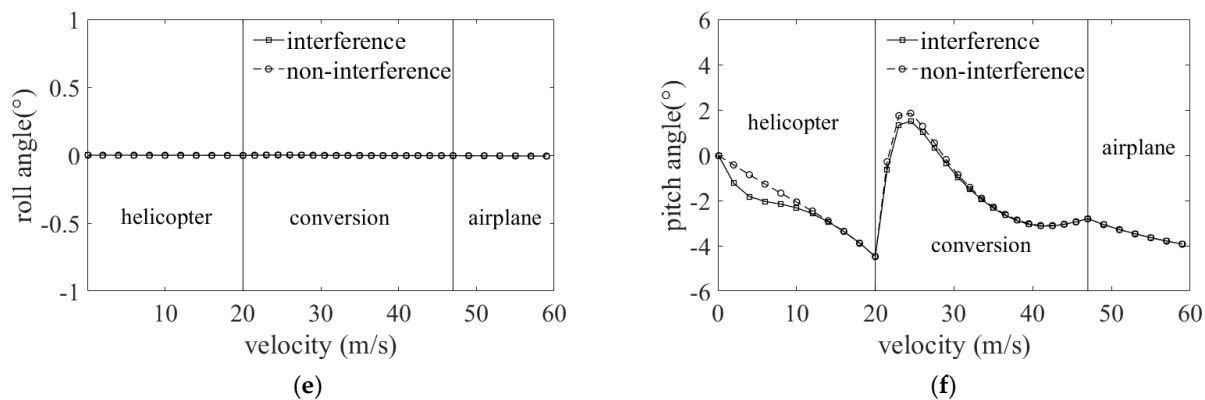


Figure 11. Comparison of trim results with and without total interference. (a) Comparison of collective stick displacement with and without interference. (b) Comparison of lateral stick displacement with and without interference. (c) Comparison of longitudinal stick displacement with and without interference. (d) Comparison of heading stick displacement with and without interference. (e) Comparison of rolling angle with and without interference. (f) Comparison of pitching angle with and without interference.

4.1. Influence on Displacement of Collective Stick

Figure 11a illustrates that the collective stick would decrease at the beginning, and then increases after 23 m/s. The aerodynamic interference would add the collective pitch in the hover and low-speed flight ranges in the helicopter mode. This is due to the additional downwash load provided by the aerodynamic interaction.

To analyze the impact weight of different aerodynamic interactions on the collective stick, the body forces and rotor thrust are calculated, as shown in Figures 12 and 13. As indicated in Figure 12a, the corresponding direction of the vertical force increment is upward in hover. As the velocity accumulates, its effect increases at first and then decreases. The maximum vertical force increment is about 13 N, which accounts for 2.2% of the weight of the vehicle. In Figure 12b, the corresponding vertical force increment caused by the rotor longitudinal interference decreases at the beginning and then increases. This is because, at low speed, the thrust increment of the front rotor is more significant than the decrement of the rear rotor. As the speed reaches a certain point, the thrust increment of the front rotor becomes smaller than that of the rear rotor, which is illustrated in Figure 13b. The maximum variation of its value is 21 N, accounting for 3.6% of the vehicle's weight. Figure 12c shows that the vertical force increment caused by the interference of the rotor–wing reaches its maximum in the hover state, which is 80 N, accounting for 13.6% of the vehicle's weight. As the flight velocity increases, the rotor wake deviates from the connected wing, decreasing the impact force of the wing. In general, the vertical force increment in the helicopter mode decreases rapidly in the helicopter mode low-speed interval. At this time, the interference of the rotor–wing plays a significant role. When the speed reaches a specific point, the vertical force increment does not change significantly, as shown in Figure 12d. At this time, the interference of longitudinal rotor–rotor plays a major role.

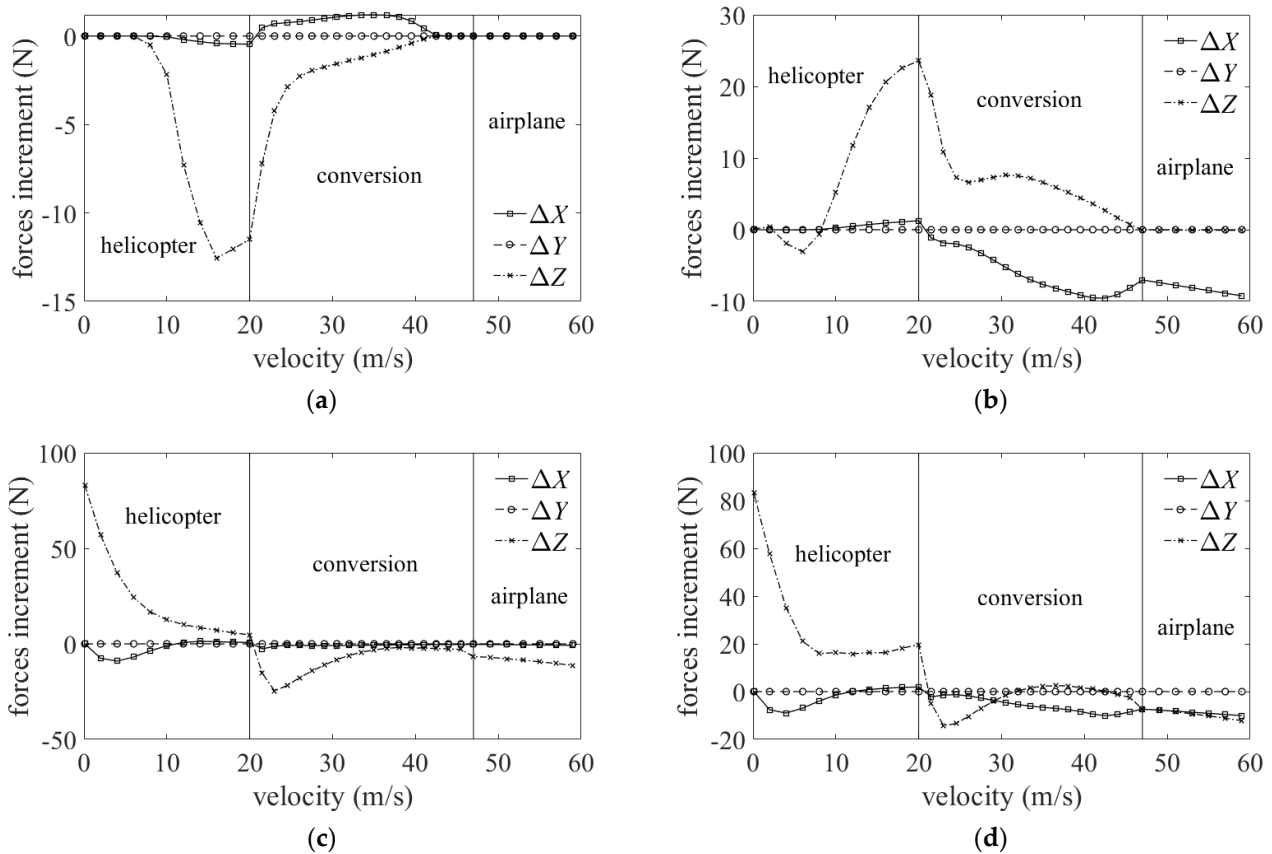


Figure 12. Influence on body forces with different interaction. (a) Body forces increment caused by rotor-lateral interaction. (b) Body forces increment caused by rotor-longitudinal interaction. (c) Body forces increment caused by rotor-wing interaction. (d) Body forces increment caused by total interaction. where $\Delta X, \Delta Y, \Delta Z$ represent the body forces increment along body axis.

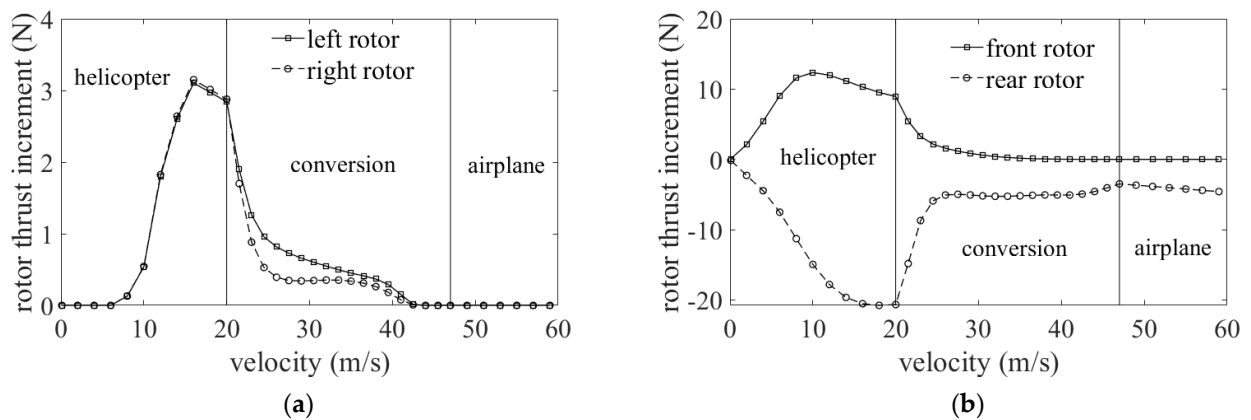


Figure 13. Influence on rotor thrust with different rotor-rotor interaction. (a) Rotor thrust increment caused by lateral interaction. (b) Rotor thrust increment caused by longitudinal interaction.

In the conversion mode, the vertical force increment caused by the interference of lateral rotor-rotor increases (Figure 12a). In contrast, the vertical force increment caused by the interference of longitudinal rotor-rotor decreases (Figure 12b). The magnitude changes rapidly at the low tilting angle and changes smoothly at the large tilting angle, and then becomes zero approaching the aircraft mode. The vertical force increment caused by the interference of the rotor-wing decreases at first and then increases (Figure 12c). The maximum variation value is about 40 N, accounting for 6.8% of the vehicle’s weight, and tends to be zero in the conversion mode with a higher tilt angle. This change is due to the

wake of the front rotor affecting the dynamic pressure of the rear wing, which leads to the change in the lift of the rear wing. In the airplane mode, the vertical force increment of the interferences caused by the lateral and longitudinal rotor–rotor are close to zero. In contrast, the interference caused by the rotor–wing will be reduced slightly.

To sum up, the influence of total interferences on the displacement of the collective stick is significant in hover and low-speed forward flight ranges. At the same time, there is little change in the velocity when the forward speed is greater than 10 m/s.

4.2. Influence on Longitudinal Trim Characteristic

The longitudinal trim characteristic of the vehicle includes the displacement of longitudinal stick and pitch angle. The aerodynamic influence on the longitudinal trim characteristic is determined by the pitch moment.

To analyze the impact weight of different aerodynamic interactions on the longitudinal stick and pitching attitude, the body moments and rotor thrust were calculated, as shown in Figures 14 and 15. As can be seen in Figure 14a, the pitch moment increment caused by the interference of the lateral rotor–rotor was relatively small, with a maximum value of 0.6 N·m. Figure 14b illustrates that the interference of the longitudinal rotor–rotor only affected the pitching moment. In the helicopter mode, due to the increase of the front rotor thrust and the decrease of the rear rotor thrust, the nose-up pitching moment of the airframe increased continuously, and its maximum value was 36 N·m. In the conversion mode, by tilting forward the rotor, the moment arm of the rotor thrusts to the centre of gravity decreased. In addition, the rotor thrust increment decreased, so did the nose-up pitching moment. In airplane mode, the nose-up moment increased slowly because of the reduction of the rotor thrust. As shown in Figure 14c, there was an additional nose-down pitching moment to the vehicle in the hover state due to the downwash flow of the rotor. Then, the nose-down pitching moment decreased with forward speed increasing. In conversion mode, the vertical force increment of the rear wing decreased and then increased, as shown in Figure 15, which resulted in an oscillating nose-down pitching moment. In airplane mode, the increased lift of the rear wing led to the nose-down moment rising. Overall, when all interferences were taken into account, as shown in Figure 14d, it would provide a nose-down moment in the hover state. The pilot would need to pull the longitudinal stick backwards. In this case, the displacement of the stick is reduced slightly. By increasing the pitching moment, the displacement of the longitudinal stick also needs to be increased in the helicopter mode. In the conversion mode, the pitching moment decreases rapidly while the tilt angle is small. The displacement of the longitudinal stick also decreases. The influence of the aerodynamic interference on the stick is not significant when $\beta_N \geq 15$ deg. In the airplane mode, the increase of nose-down pitching moment results in the reduction of the longitudinal stick displacement.

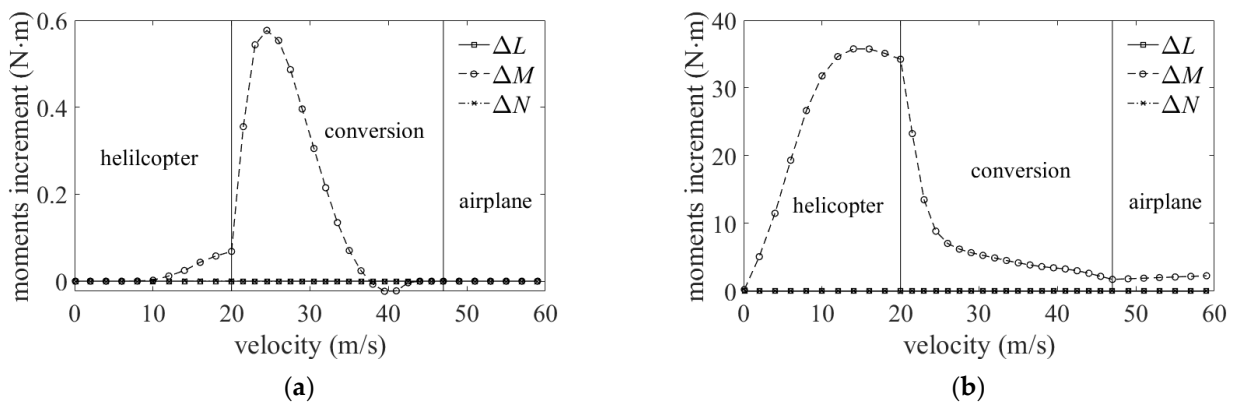


Figure 14. Cont.

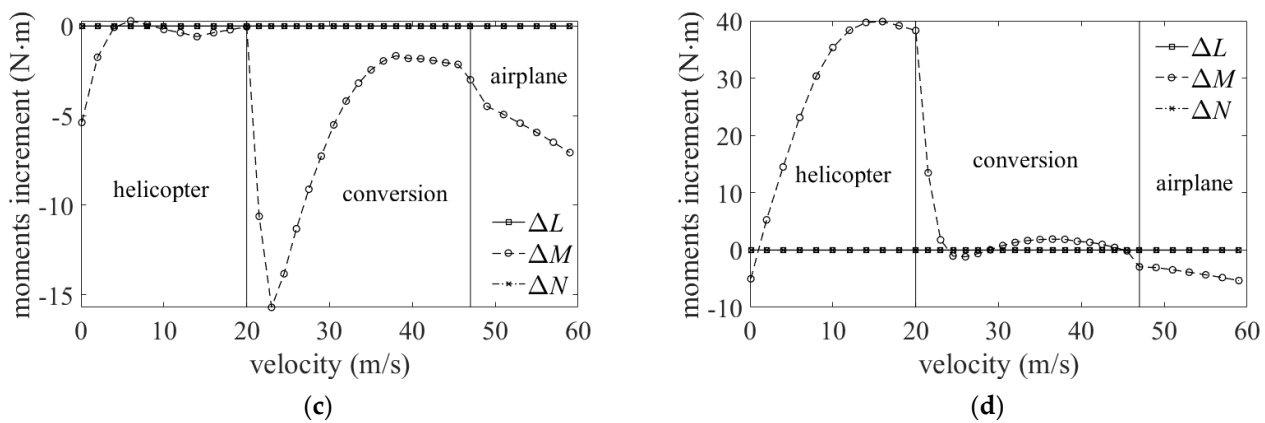


Figure 14. Influence on body moments with different interaction. (a) Body moments increment caused by rotor lateral interaction. (b) Body moments increment caused by rotor longitudinal interaction. (c) Body moments increment caused by rotor–wing interaction. (d) Body moments increment caused by total interaction. where ΔL , ΔM , ΔN represent the body moments increment along body axis.

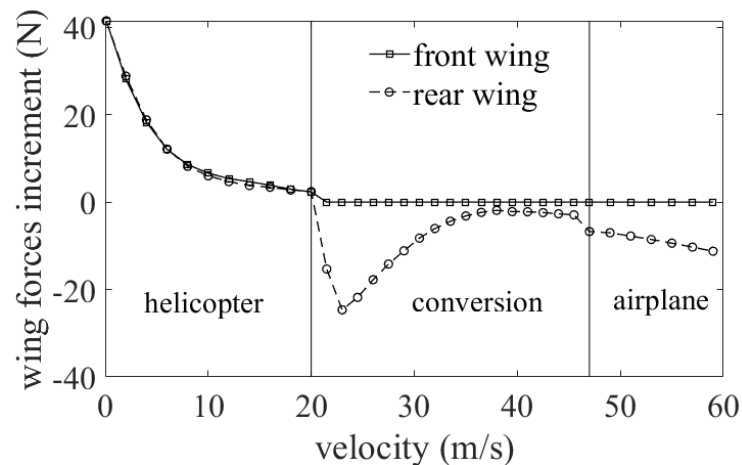


Figure 15. Vertical forces increment of front and rear wings caused by rotor–wing interaction.

Figure 11f shows that the pitching attitude decreased in the helicopter mode. The vehicle needs to change the pitching attitude to make gravity create the longitudinal force to balance the aircraft. The additional drag caused by the interference increased at the beginning and then decreased, as shown in Figure 12d. Therefore, the vehicle will first pitch down faster, and then the trend of variation will slow down compared to non-interaction. In the conversion mode, the pitching attitude first increased and decreased later. The reason is that the forward longitudinal force generated by the rotor is more remarkable as the tilt angle increases. The aircraft needs to raise its nose so that the longitudinal component of gravity transforms to the drag to balance the body. When the tilt angle increases to a particular value, the thrust of the rotor and pitching attitude decreases rapidly with velocity increases. Since the interference will increase the drag of the vehicle, the pitching attitude is smaller than the case where the interference is not considered. In the airplane mode, the aircraft is in the state of nose-down, and its pitching attitude keeps decreasing as the speed increases. It is because the wing has an initial incidence. As the dynamic pressure increases, the vehicle needs to reduce the wing angle of attack to balance gravity.

5. Conclusions

In this paper, the calculation methods of aerodynamic interaction in the QTR are developed. Then an integrated modelling approach was developed for corresponding flight dynamics analysis. A mixed control strategy was proposed to combine multiple

redundant control inputs. Based on this strategy, the trim characteristics of the QTR were investigated. Additionally, the influence of different types of aerodynamic interference on the trim characteristic was analyzed. The following conclusions can be obtained:

1. The interference of lateral rotor–rotor has little influence on the body forces and moments. The maximum variation of the vertical force increment is 13 N, which accounts for 2.2% of the vehicle’s weight. On the other hand, the interference of the longitudinal rotor–rotor mainly affects the vertical force and pitching moment. The maximum vertical force increment is 21 N, which accounts for 3.6% of the overall weight. In addition, the nose-up pitching moment varies greatly, with a maximum value of 36 N·m;
2. The interference of the rotor–wing mainly affects the vertical force and pitching moment. The variation of the vertical force increment reaches its maximum in the hover state, accounting for 13.6% of the vehicle’s weight. At this time, a nose-down pitching moment of about 5 N·m will be generated. The pitching moment will be changed significantly in the conversion mode, and the corresponding maximum pitching moment is 15 N·m.
3. The trim values of the longitudinal stick and the pitching angle are affected significantly by rotor–rotor and rotor–wing interference in the helicopter mode and conversion mode with a lower tilt angle. The interaction also affects the longitudinal stick in the airplane mode and the collective stick at low-speed range in the helicopter mode.

Author Contributions: Conceptualization, P.Z. and R.C.; methodology, P.Z.; software, P.Z.; validation, P.Z., Y.Y. and C.C.; formal analysis, P.Z.; investigation, P.Z. and Y.Y.; resources, P.Z.; data curation, P.Z.; writing—original draft preparation, P.Z.; writing—review and editing, Y.Y. and C.C.; visualization, P.Z.; supervision, R.C. and Y.Y.; project administration, R.C.; funding acquisition, R.C. All authors have read and agreed to the published version of the manuscript.

Funding: This research received no external funding.

Institutional Review Board Statement: Not applicable.

Informed Consent Statement: Not applicable.

Data Availability Statement: Not applicable.

Conflicts of Interest: The authors declare no conflict of interest.

References

1. Braganca, E. The V-22 Osprey: From Troubled Past to Viable and Flexible Option. *Jt. Force Q.* **2012**, *66*, 80–84.
2. King, D. A System Engineering Approach to Carefree Maneuvering in The BA609. In Proceedings of the American Helicopter Society 61st Annual Forum, Grapevine, TX, USA, 1–3 June 2005.
3. Snyder, D. The Quad Tiltrotor: Its Beginning and Evolution. In Proceedings of the International Powered Lift Conference, Arlington, VA, USA, 30 October–1 November 2000.
4. Marr, R.; Blackman, S.; Weiberg, J.; Schroers, L.G. Wind tunnel and flight test of the XV-15 Tilt Rotor Research Aircraft. In Proceedings of the 35th Annual National Forum, Washington, DC, USA, 21–23 May 1979.
5. Radhakrishnan, A.; Schmitz, F. Quad Tilt Rotor Aerodynamics in Ground Effect. In Proceedings of the AIAA Applied Aerodynamics Conference, Toronto, ON, Canada, 5–8 June 2006.
6. Muraoka, K.; Okada, N.; Kubo, D. Quad Tilt Wing VTOL UAV: Aerodynamics Characteristics and Prototype Flight Test. In Proceedings of the Aerospace Conference, Seattle, WA, USA, 7–14 March 2009.
7. Yuan, Y.; Chen, R.; Li, P. Trim investigation for coaxial rigid rotor helicopters using an improved aerodynamic interference model. *Aerosp. Sci. Technol.* **2019**, *85*, 293–304. [[CrossRef](#)]
8. Ji, H.; Chen, R.; Lu, L.; White, M.D. Pilot workload investigation for rotorcraft operation in low-altitude atmospheric turbulence. *Aerosp. Sci. Technol.* **2021**, *111*, 106567. [[CrossRef](#)]
9. Li, P.; Chen, R. A Mathematical Model for Helicopter Comprehensive Analysis. *Chin. J. Aeronaut.* **2010**, *23*, 320–326.
10. Sheng, C.; Narramore, C.J. Computational Simulation and Analysis of Bell Boeing Quad Tiltrotor Aero Interaction. *J. Am. Helicopter Soc.* **2009**, *54*, 42002. [[CrossRef](#)]
11. Patrick, P.; Andreas, K.; Damien, D.; Breitsamter, C. Numerical Investigation of an Optimized Rotor Head Fairing for the RACER Compound Helicopter in Cruise Flight. *Aerospace* **2021**, *8*, 66.

12. Shi, Y.; Li, G.; Su, D.; Xu, G. Numerical Investigation on ship/multi-helicopter dynamic interface. *Aerosp. Sci. Technol.* **2020**, *106*, 106175. [[CrossRef](#)]
13. Ferguson, S. *A Mathematical Model for Real Time Flight Simulation of a Generic Tilt-Rotor Aircraft*; NASA CR-166536; NASA: Washington, DC, USA, 1988.
14. Ostroff, J.; Downing, D.; Rood, W. *A Technique Using a Nonlinear Helicopter Model for Determining Trims and Derivatives*; NASA Technical Note D-8159; NASA: Washington, DC, USA, 1976.
15. Johnson, W. *Influence of Lift Offset on Rotorcraft Performance*; NASA/TP-2009-215404; NASA: Washington, DC, USA, 2009.
16. Yan, X.; Chen, R. Control strategy optimization of dynamic conversion procedure of tiltrotor aircraft. *Acta Aeronaut. Astronautica Sinica* **2017**, *38*, 520865.
17. Wang, Z.; Li, J.; Duan, D. Manipulation Strategy of Tilt Quad Rotor Based on Active Disturbance Rejection Control. *J. Aerosp. Eng.* **2020**, *234*, 573–584. [[CrossRef](#)]
18. Talbot, P.; Tinling, B.; Decker, W. *A Mathematical Model of a Single Main Rotor Helicopter for Piloted Simulation*; NASA Technical Memorandum 84281; NASA: Washington, DC, USA, 1982.
19. Chen, R. *A Simplified Rotor System Mathematical Model for Piloted Flight Dynamics Simulation*; NASA Technical Memorandum 78575; NASA: Washington, DC, USA, 1979.
20. McCroskey, W.; Spalart, P.; Laub, G.; Maisel, M.; Maskew, B. *Air Loads on Bluff Bodies, with Application to the Rotor-Induced Downloads on Tiltrotor Aircraft*; NASA-TM-84401; NASA: Washington, DC, USA, 1983.
21. Carlson, E.; Zhao, Y. Optimal short takeoff of tiltrotor aircraft in one engine failure. *J. Aircr.* **2002**, *39*, 280–289. [[CrossRef](#)]
22. Wang, J.; Yu, Z.; Chen, R.; Wang, Z.; Lu, J. Aerodynamic characteristics of quad tilt rotor aircraft in vertical flight. *J. Aerosp. Power* **2021**, *36*, 249–263.
23. Ji, H.; Chen, R.; Li, P. Real-time simulation model for helicopter flight task analysis in turbulent atmospheric environment. *Aerosp. Sci. Technol.* **2019**, *92*, 289–299. [[CrossRef](#)]
24. Maisel, M. *The History of the XV-15 Tilt Rotor Research Aircraft from Concept to Flight*; NASA SP-2000-4517; NASA: Washington, DC, USA, 2000.